Check for updates

Tuning shape and internal structure of protein droplets *via* biopolymer filaments†

Danielle R. Scheff, [ab] Kimberly L. Weirich, *[acd] Kinjal Dasbiswas, [e] Avinash Patel,[cf] Suriyanarayanan Vaikuntanathan[ag] and Margaret L. Gardel *[abcd]

Macromolecules can phase separate to form liquid condensates, which are emerging as critical compartments in fields as diverse as intracellular organization and soft materials design. A myriad of macromolecules, including the protein FUS, form condensates which behave as isotropic liquids. Here, we investigate the influence of filament dopants on the material properties of protein liquids. We find that the short, biopolymer filaments of actin spontaneously partition into FUS droplets to form composite liquid droplets. As the concentration of the filament dopants increases, the coalescence time decreases, indicating that the dopants control viscosity relative to surface tension. The droplet shape is tunable and ranges from spherical to tactoid as the filament length or concentration is increased. We find that the tactoids are well described by a model of a quasi bipolar liquid crystal droplet, where nematic order from the anisotropic actin filaments competes with isotropic interfacial energy from the FUS, controlling droplet shape in a size-dependent manner. Our results demonstrate a versatile approach to construct tunable, anisotropic macromolecular liquids.

Introduction

Liquid condensates, dense macromolecular droplets that phase separate out of a dilute suspension, are widespread in soft and biological materials ranging from coacervates[1] to membrane-less organelles.[2] The formation and material properties of condensates can be tuned through modifying macromolecular composition[3–5] or environmental conditions.[6–8] Intriguingly, the fluid condensates typically adopt a characteristic spherical shape and coalescence over time, indicative of droplets composed of an isotropic liquid with a dominant interfacial tension. However, macromolecules are inherently structured, often with significant rigidities and size, which may impart anisotropy to these liquids.

It is well appreciated that highly anisotropic rod-like objects can form structured liquid phases.[9,10] Below a critical volume fraction, a suspension of rods is isotropic. However, above a critical packing the rods locally align due to entropic effects and adopt orientational order, forming a phase known as a nematic liquid crystal.[10] The local alignment imparts an elasticity to the fluid,[11] which can depend on the packing and properties of the rods.[12,13] Liquid crystal droplets are observed to nucleate out of a dense isotropic suspension at the isotropic–nematic phase transition[14–16] or out of dilute suspensions through the addition of depletants or cross-links.[17–19] The competing effects of elasticity and surface tension in the droplets results in an elongated, spindle shape called a tactoid.[20] Due to different scaling of bulk and interfacial properties, the droplet shape is size-dependent[14,15] and is predicted to transition from spherical to tactoid.[20,21] Tactoids have been observed to form from a range of anisotropic components, including fd virus, biopolymer filaments, carbon nanotubes, and inorganic oxides.[14,15,19,22–25] Recently, nematic droplets with tunable shape were achieved by inducing attraction of biopolymer filaments of actin with transient cross-links.[19] The extent to which rod-like components influence anisotropic properties of condensates such as protein-based droplets remains to be explored.

Here we create composite liquid droplets composed of FUS, a protein that forms condensates,[26] doped with filaments of the biopolymer actin to investigate the impact of anisotropic dopants on droplet shape and properties. We find that actin incorporates throughout FUS droplets, leading to a composite liquid phase. By varying actin filament concentration and

*a James Franck Institute, University of Chicago, Chicago, IL 60637, USA.
E-mail: kweirich@uchicago.edu, gardel@uchicago.edu*

b Department of Physics, University of Chicago, Chicago, IL 60637, USA

c HHMI HCIA Summer Institute, Marine Biological Laboratory, Woods Hole, MA 02543, USA

d Pritzker School of Molecular Engineering, University of Chicago, Chicago, IL 60637, USA

e Department of Physics, University of California, Merced, CA 95343, USA

f Dewpoint Therapeutics GmbH, Pfotenhauer Strasse 108, Dresden 01307, USA

g Department of Chemistry, University of Chicago, Chicago, IL 60637, USA

† Electronic supplementary information (ESI) available. See DOI: 10.1039/c9sm02462j

length, the degree of the anisotropic effects on the liquid vary and result in tunable droplet shape. We find that the droplet shape is well described by a continuum model of a nematic droplet, where the nematic elastic energy arises from the actin filaments. Our results indicate that rigid dopants can impart liquid crystallinity to otherwise isotropic droplets. Such composite droplets provide a new means to control material properties and shape of liquid condensates, with implications for designing both biological assemblies and soft materials.

Methods

Protein purification

Monomeric actin (G-actin) is purified from rabbit skeletal muscle acetone powder (Pel Freeze Biologicals, Product code: 41008-3) using a procedure adapted from ref. 27 and stored in 2 mM Tris, 0.2 mM ATP, 0.5 mM DTT, 0.1 mM $CaCl_2$, 1 mM NaN_3, pH 8. Actin is labelled using tetramethylrhodamine-6-maleimide (TMR) dye (Life Technologies). HisTag mouse capping protein is purified from bacteria using a procedure adapted from ref. 28 and stored in a buffer composed of 10 mM Tris, 40 mM KCl, 0.5 mM DTT, 0.01 wt% NaN_3, 50 vol% glycerol, pH 7.5. FUS-GFP is expressed in and purified from insect cells as described in ref. 26 and stored in a buffer composed of 2 mM Tris, 500 mM KCl, 1 mM DTT, pH 7.4. All proteins are flash frozen in liquid nitrogen and stored at $-80\ ^{\circ}C$. Actin and capping protein are used within three days of thawing, while FUS is used within 4 hours. After thawing, proteins are stored at 0–$4\ ^{\circ}C$ until use.

Experimental assay

The experimental chamber is composed of a glass cylinder (3166-10; Corning Life Sciences) epoxied to a glass coverslip (Fisherbrand, #1.5). The coverslip surface is passivated against protein adhesion through an oil–surfactant layer. To form the layer, 2 wt% of the surfactant, PFPE-PEG-PFPE (008; RAN Biotechnologies) is first dissolved in Novec-7500 Engineered Fluid (3M). The oil–surfactant solution is sonicated for 30 min in a bath sonicator, filtered through a 0.2 μm pore sized membrane (6784-1302; GE Healthcare), then flushed with nitrogen gas and stored at $4\ ^{\circ}C$ until use. Coverslips are first cleaned by sonicating in ethanol, then immersed in 2 vol% triethoxy(octyl)silane (440213; Sigma-Aldrich) in isopropanol for 10 min, submerged 24 times in water to rinse, and dried overnight at $30\ ^{\circ}C$ to form a silane layer. Immediately prior to adding the sample, 4 μL of oil–surfactant solution is added to the sample chamber to create a thin layer of oil–surfactant at the coverslip. After coating the coverslip, excess solution is removed.

To polymerize actin filaments, 5 μM actin monomer (0.5 μM labelled with TMR) is added to a buffer composed of 2 mM Tris, 2 mM $MgCl_2$, 25 mM KCl, 0.5 mM ATP, 0.3 wt% methylcellulose, pH 7.4. To regulate actin filament length, capping protein is added to the final concentration of 50–150 nM. The actin is incubated for at least 30 min, while it polymerizes into filaments, before 0.25 μM phalloidin is added to prevent dilution-induced depolymerization. Actin filaments are then mixed with 4.4 μM FUS resulting in a final mixture composed of 2 mM Tris, 2 mM $MgCl_2$, 45 mM KCl, 0.5 mM ATP, 0.04 mM DTT, 0.3 wt% methylcellulose, 0.1 μM phalloidin. This mixture is immediately added to the sample chamber. Samples are incubated for 60 min before images are collected for droplet shape analysis.

Filament length

We modulate the length of actin filaments through capping protein, which binds to growing filaments and prevents further polymerization, leading to an exponential distribution of filament lengths.[29] In the limit of strong binding, we approximate the average number of monomers in a filament from the ratio of actin monomers to capping protein, [Actin]/[Capping Protein]. We convert monomers to length using the known value of $\sim$1 monomer per 2.7 nm in a filament, leading to average filament length of 2.7 nm $\times$ [Actin]/[Capping Protein].[19] Pre-polymerizing the actin and stabilizing with phalloidin before mixing with FUS minimizes the influence of interactions between FUS and actin on actin filament polymerization and filament length. To further reduce artifacts associated with filament length, samples are compared only with other samples prepared on the same day when measuring the effect of actin and capping protein concentration. For measurements taken at different actin concentrations, the actin filaments in each sample are sourced from the same pre-polymerized stock. For different capping protein concentrations, all samples use capping protein sourced from the same aliquot.

Microscopy

Samples are imaged using a spinning disk confocal microscope (Nikon, Yokogawa) equipped with a CMOS camera (Andor) and 60 × 1.2NA objective (Nikon). Samples are illuminated using a 491 or 561 nm laser (cobolt). The polarization images were acquired on a home built LC-Polscope microscope constructed by Rudolph Oldenbourg at Marine Biological Laboratory in Woods Hole, MA.[30]

Image analysis

Droplet aspect ratio is calculated from droplet shape parameters extracted through ImageJ's built-in Analyze Particles function.[31,32] Images are thresholded and droplets in contact with another droplet or in the process of coalescing are excluded through visual inspection. Due to uneven illumination, droplets near the image edge may appear misshapen after thresholding; these droplets are similarly excluded. To extract the major and minor axes lengths, droplet shape is approximated as an ellipsoid. Droplet shape classification as tactoids or ellipsoids is determined through visual inspection of all droplets in a given field of view, excluding only those whose shape could not be confidently classified.

To estimate the amount of actin that partitions into droplets, the relative intensities inside to outside the droplet is calculated from images which have been background corrected by subtracting a dark image. Dark is defined as the average intensity without

Soft Matter

Paper

illumination, representing the camera dark levels. The average intensity inside of droplets is compared to the intensity within a ring between 1.4 and 3.2 μm from the droplet border, excluding anywhere within 1.4 μm of another droplet. The ratio between these values is calculated separately for each droplet to account for difference in illumination across the field of view. This ratio is then averaged across all measured droplets.

Quasi bipolar tactoid model

The spindle shape of the tactoid is described naturally by a bipolar geometry obtained as surface of revolution of a circular arc about its chord, which corresponds to the major axis of the tactoid.[20,33] The size and shape of the tactoid is then completely prescribed by the length of its semi-major axis, R, and semi-minor axis, r, which together define the aspect ratio, R/r (Fig. 5a). This parameter can vary from $R/r = 1$ for a spherical droplet to larger values for more elongated droplets. Since we observe relatively spheroidal droplets ($R/r < 2.5$), we choose to work within the quasi bipolar tactoid model introduced in ref. 34, where the nematic director lines, which follow the local average orientation of the comprising rods, meet "virtually" at points outside the droplet at a distance $2\tilde{R}$ apart (Fig. 5a). When, $R = \tilde{R}$, we have the idealized bipolar tactoid configuration which arises only in the limit of very strong surface anchoring of the director to the tactoid surface. For the rest of this discussion, we define the parameters, $x \equiv R/r$ as the aspect ratio, and $y \equiv \tilde{R}/R$, the extent of the bipolarity of the director field. The optimal shape and director configuration of the droplet is then decided by a minimization of its total free energy with respect to these parameters.

If a nematic droplet is large relative to the scale of the comprising rods (here short, actin filaments), its free energy can be written as a sum of an elastic and a surface energy. This latter contains contributions from both the isotropic surface tension of the nematic fluid as well as the anisotropic surface tension or surface anchoring of the director to the droplet surface, γ_A. For the quasi bipolar tactoid model, we can scale out the size scale of the droplet (given by its semimajor axis, R) and write the total free energy in terms of the aspect ratio, x, and bipolarity parameter, y, as,

$$F(R;x,y) = KRf_{el}(x,y) + \gamma R^2(f_s(x) + \omega f_{an}(x,y)), \quad (1)$$

where K is the nematic elastic constant, γ is the surface tension associated with the droplet interface and ω is a dimensionless anchoring strength. The surface anchoring energy is defined as the energy cost of misalignment of the director, $\hat{n}$, with the surface described by its normal, $\hat{N}$, such that the total anchoring free energy over the whole surface, S is, $\gamma_A \int_s ds(\hat{n} \cdot \hat{N})^2$, with $\omega = \gamma_A/\gamma$. Further, we use the equal Frank elastic constant approximation for bend and splay and the saddle-splay term allowed for a finite surface is ignored since this just renormalizes the usual splay constant.[34] Although the bend and splay constants are in principle different,[20] the equal constant approximation reduces the number of free fitting parameters in the model and captures the trends in droplet shape *versus* size. The volume of the tactoid similarly scales as $R^3 v(x)$.

These nondimensional shape factors, corresponding to surface tension, nematic elastic, and surface anchoring energy as well as the volume are calculated for the quasi bipolar geometry. This is done in the bispherical coordinate system (detailed in ref. 34 and 35) with coordinates $0 < \phi < 2\pi$, $0 < \xi < \pi$, $0 < \eta < \eta_0$, where $\eta_0 = 2\tan^{-1}(1/x)$ is related to the aspect ratio of the tactoid. The corresponding scale factors in the bispherical coordinate system are defined as: $h_\phi = Z^{-1}\sin\xi\sin\eta$, $h_\xi = Z^{-1}$, $h_\eta = Z^{-1}\sin\xi$ with $Z \equiv 1 + \sin\xi\cos\eta$. The shape factors defined in eqn (1) can be calculated in this coordinate system by performing the following integrals. Here we give the results directly based on the derivation given in ref. 34.

$$f_s(x,y) = \int_0^{2\pi} d\phi \int_0^\pi d\xi (h_\phi h_\xi)|_{\eta=\eta_0}$$
$$= 2\pi/x^2 \cdot (x + x^3 - (x^4 - 1)\tan^{-1}x^{-1}), \quad (2A)$$

$$f_{el}(x,y) = \int_0^{2\pi} d\phi \int_0^\pi d\xi \int_0^{\eta_0} d\eta h_\phi h_\xi h_\eta N^{-1} \cdot (4\cos^2\xi + \sin^2\xi\cos^2\eta) \quad (2B)$$

$$f_{an}(x,y) = \int_0^{2\pi} d\phi \int_0^\pi d\xi (h_\phi h_\xi)|_{\eta=\eta_0} (4N)^{-1} \cdot (y^2 - 1)^2 \cos^2\xi\sin^2\eta_0 \quad (2C)$$

$$v(x) = \int_0^{2\pi} d\phi \int_0^\pi d\xi \int_0^{\eta_0} d\eta h_\phi h_\xi h_\eta$$
$$= \pi/(2x^3) \cdot (x + 2/3x^3 + x^5 - (x^2 - 1)(x^2 + 1)^2 \tan^{-1}x^{-1}), \quad (2D)$$

with the factor N defined as,

$$N \equiv (\sin\xi\cos\eta + (1 + \sin\xi\cos\eta) \cdot (y^2 - 1)/2)^2 + y^2\sin^2\xi\sin^2\eta,$$

where the factors corresponding to surface area and volume can be calculated analytically in closed form, while those related to the nematic elastic energy and the anchoring energy are calculated by numerically integrating the expressions in (2B) and (2C). It is readily checked that in the spherical limit, $x \to 1$, we recover the expected surface area and volume factors, and that in the elongated or high aspect ratio limit, $x \to \infty$, the surface area and volume scale as $R^2/x \sim R \cdot r$ and $R^3/x^2 \sim R \cdot r^2$ as expected for a cylindrical limit.

We now consider a tactoid of given volume, V, and find the shape parameters, x and y that minimize the total free energy. The free energy in eqn (1) can be re-expressed in terms of the tactoid volume and aspect ratio, by using $R = (V/v(x))^{\frac{1}{3}}$, and expressed as a nondimensional free energy, $F(x,y,R)\left/\left(\gamma V^{\frac{2}{3}}\right)\right.$, which depends on the tactoid aspect ratio and two nondimensional parameters: $K/(\gamma V^{1/3})$, expressing the relative importance of the bulk nematic and surface tension energies, and ω. The equilibrium shape, and therefore the aspect ratio, of a tactoid of a given volume, V, and given material properties, K, γ, ω is found by numerically minimizing the nondimensional free

energy with respect to the shape parameters, x and y. We employ standard numerical minimization techniques from the Mathematica FindMinimum function.

We then compare the equilibrium aspect ratio *vs.* tactoid size (in terms of the cross-sectional area which scales as $V^{2/3}$) for different values of the length scale, K/γ and the dimensionless parameter ω, to the corresponding experimentally measured values. By inspection, we choose three different curves for three different K/γ and ω values that best describe and bound the data set obtained from averaging over the aspect ratio and area measurements of populations of tactoids. These fitting curves along with the experimental data are shown in Fig. 5c and Fig. S1 (ESI†). We note that not all tactoids in the same experiment have the same material properties. We thus obtain a range of K/γ and ω values for each experiment at a different capping protein concentration.

Results and discussion

To investigate the impact of anisotropic components such as biopolymer filaments on protein droplets, we sought to form composite droplets out of FUS and actin filaments. The RNA-binding protein, FUS, is known to liquid–liquid phase separate into a protein-rich condensed phase upon a reduction in monovalent ion concentration.[26] Here, we form composite FUS–actin droplets by adding 4.4 µM FUS-GFP (FUS) to a solution containing pre-polymerized, fluorescent actin filaments (1 µM monomeric actin labeled with TMR, 3 mol% capping protein), which reduces the ambient monovalent salt concentration by an order of magnitude upon mixing, from 500 mM to 45 mM KCl (Fig. 1a). Using fluorescence microscopy, we observe micrometer-sized condensates enriched with FUS, consistent with previous reports of FUS droplets.[26] Additionally, we find these droplets are also enriched with actin (Fig. 1b). We find that the actin fluorescence uniformly colocalizes with the FUS fluorescence, indicating that these two proteins form composite droplets with apparent homogeneous distribution of both actin and FUS (Fig. 1c). When we first observe FUS droplets (~10 min after mixing), they already contain concentrated actin, demonstrating that actin partitions into droplets relatively rapidly.

To quantify the partitioning of actin into the droplets, we compare the average actin intensity in the droplet interior, I_{inside}, to exterior, $I_{outside}$. Since fluorescence intensity is proportional to protein concentration, the intensity ratio, $I_{inside}/I_{outside}$, provides an estimate of the actin concentration inside the droplets relative to in the bulk solution.[36,37] At low actin concentrations (0.01 µM), the intensity of actin inside is about 7 times greater than in the bulk, indicating that the actin filaments preferentially accumulate into FUS droplets. At higher actin concentrations (0.1–1 µM), the intensity is ~25–40 times greater in the droplets than the bulk solution (Fig. 1d). These observations are consistent with previous measurements of actin partitioning into coacervates, where the intensity ratio was found to increase with increasing actin at low concentrations before plateauing at higher concentrations.[37]
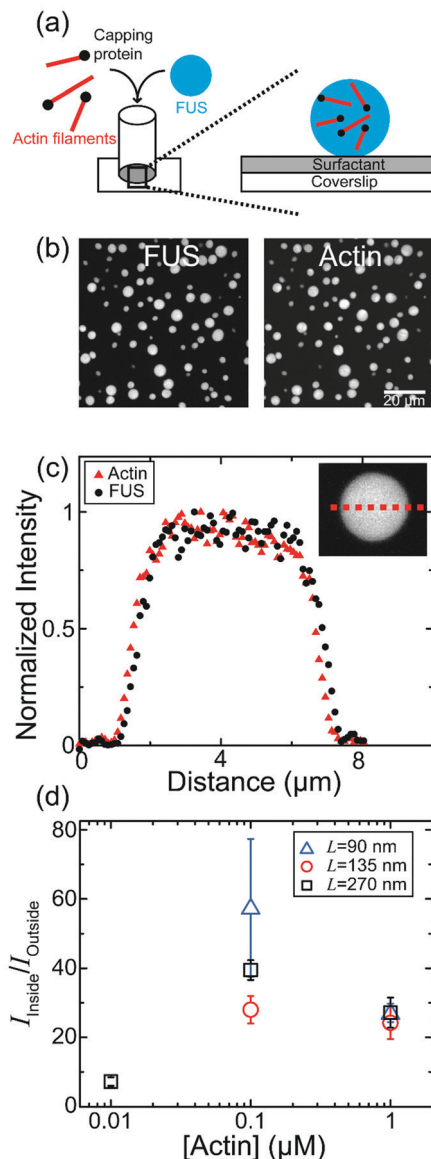

Fig. 1 Actin and FUS form composite droplets (a) Schematic of experimental setup. The protein FUS mixes with short, pre-polymerized actin filaments to form composite droplets which sediment to a surfactant passivated layer at the bottom of the sample chamber. (b) Images of composite droplets through fluorescence microscopy of FUS (left) and actin (right). Scale bar is 20 µm (c) Intensity across the midplane of a droplet (inset, red dashed line) for FUS (black circles) and actin (red triangles). Intensities are normalized by their maximum values. Data shown in (b) and (c) for samples containing 1 µM actin with length $L \sim 90$ nm. (d) Intensity of actin in droplets relative to in the solution as a function of actin concentration for samples with actin of length $L \sim 90$ nm (blue triangles), $L \sim 135$ nm (red circles), and $L \sim 270$ nm (black squares). Error bars are standard deviation between droplets. In all panels, the data shown are droplet samples composed of 4.4 µM FUS.

We note that without knowing the explicit relationship between intensity and concentration, the ratio $I_{inside}/I_{outside}$ does not provide an exact measure of a partition coefficient. However, the large value measured is indicative of large accumulation of actin within the droplets. Thus, actin filaments preferentially incorporate into the FUS droplets across a range of actin concentrations.
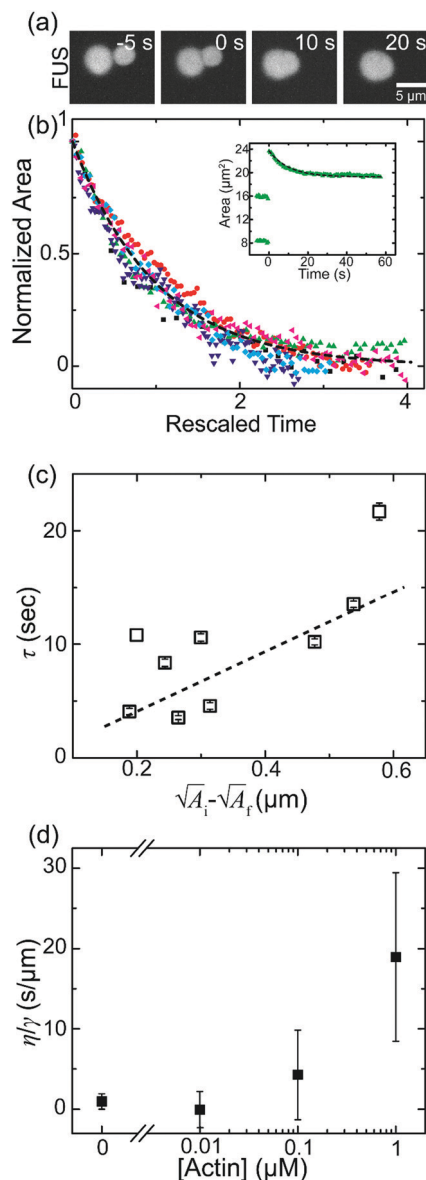
Fig. 2 Droplets are liquid with actin dependent properties. (a) Fluorescence microscopy images of (FUS-labeled) droplets coalescing over time. Scale bar is 5 μm. (b) Inset: Area over time for a single coalescence event (green triangles) is fit by a single exponential (black dashed line). Normalized area for 6 different droplet coalescence events with time rescaled by the time-scale τ. Black dashed line indicates a single exponential, e^{-t}. Data shown is for droplets composed of 4.4 μM FUS and 1 μM actin with $L \sim 90$ nm. (c) Dependence of the characteristic coalescence time, τ, on the coalescence length scale, defined as the difference of the square roots of the final and initial areas. Dashed line indicates a linear fit to the data. Data shown are droplet samples composed of 4.4 μM FUS and 1 μM actin. (d) The ratio of the viscosity to surface tension as a function of actin concentration. Error bars are the standard error from the linear fit.

Similar to previous reports of FUS droplets,[26] one growth mechanism of composite actin–FUS droplets is coalescence, where two initially separate droplets merge and relax into a new droplet (Fig. 2a and Movie S1, ESI†) Analyzing the dynamics of coalescence provides an estimate of the relative contributions of two droplet material properties: interfacial tension and viscosity.

We measure the droplet cross-sectional area, A, as a function of time, t, during individual coalescence events (Fig. 2b, inset). Two droplets with a total initial cross-sectional area at time of first contact, A_i, coalesce into a new droplet which relaxes to a final shape with cross-sectional area, A_f. The area decrease is consistent with an exponential decay, which we can extract a characteristic relaxation time, τ, from the fit $A(t) = A_f + (A_i - A_f)e^{-t/\tau}$. Plotting the normalized area, $(A - A_f)/(A_i - A_f)$, against rescaled time, t/τ, reveals that coalescence events from various droplet sizes collapse into a single curve that is consistent with an exponential decay (Fig. 2b), indicative of coalescence associated with isotropic fluids.[19]

For isotropic fluids, we expect the characteristic relaxation time, τ, to scale linearly with the coalescence relaxation length, the difference between the initial and final length, Δl, of the droplet. Here, to account for droplets with shapes that deviate from spherical, we define the relaxation length from the square root of the droplet cross-sectional area such that $\Delta l = \sqrt{A_i} - \sqrt{A_f}$. We find that τ increases with the difference between the coalescence relaxation length (Fig. 2c). By balancing viscously dissipated mechanical energy against change in the interfacial energy of the coalesced droplet as it relaxes, we see that τ depends on the viscosity, η, and interfacial tension, γ, of the liquid as $\tau \sim \eta/\gamma \cdot \Delta l$.[19] Thus, the slope of the linear fit in Fig. 2c gives the ratio η/γ. In Fig. 2d, we find η/γ increases with actin concentration, suggesting that actin filament density impacts composite droplet viscosity more than it affects surface tension.

In contrast to FUS droplets which are always spherical,[26] composite droplets also adopt a variety of elongated shapes (Fig. 3a). The shape of these droplets is dependent both on the droplet size and actin concentration (Fig. 3b). While average droplet size increases with time as droplets coalesce (Movie S2, ESI†), we note that the droplet shape at a given size is independent of the time after formation, suggesting rapid actin accumulation in the droplets. Despite this observation, to reduce measurement uncertainty, we investigate the dependence of droplet shape in a population of droplets at a given time after formation. For low actin concentrations (<0.1 μM), droplets of all assayed cross-sectional areas (between 1 μm^2 and 32 μm^2) are spherical. However, for actin concentrations greater than 0.1 μM, we observe non-spherical droplets, particularly in smaller (below ~ 15 μm^2) droplets. For 1 μM actin, elongated shapes are observed for droplet sizes smaller than ~ 20 μm^2; as the droplet size increases, the average aspect ratio approaches 1 (Fig. 3c). To quantitatively compare the size and actin concentration dependence of droplet shape, we plot average aspect ratio for small (4–6 μm^2), medium (14–16 μm^2) and large (>20 μm^2) droplets. We find the average aspect ratio decreases as droplet size increases, with the trend most pronounced at the highest actin concentration (1 μM). Furthermore, the average aspect ratio increases with actin concentration (Fig. 3d). In contrast to the elongated droplets observed at higher concentrations, for the lowest actin concentration (0.01 μM), droplets of all sizes have an aspect ratio ~ 1. This strongly suggests that the high density of filaments within the droplets underlie the observed differences in aspect ratio.
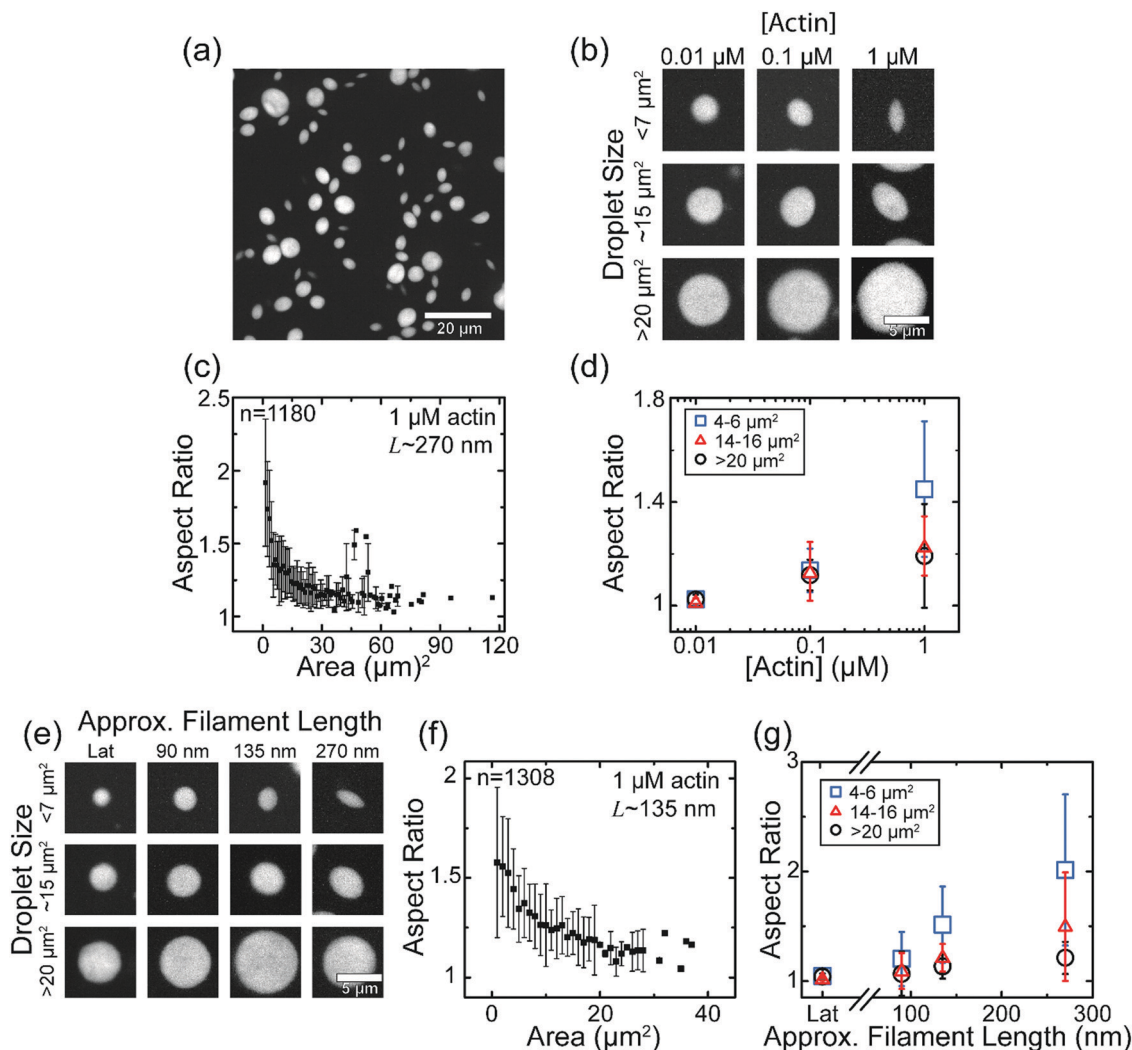
Fig. 3 Actin filaments elongate droplets. (a) Fluorescence microscopy image of FUS-labeled droplet samples containing 1 μM actin with $L \sim 270$ nm. Scale bar is 20 μm. (b–d) Higher actin concentration elongates droplets. All data shown for droplets containing filaments with $L \sim 270$ nm. (b) Fluorescence images of composite droplets as a function of droplet size and actin concentration. Scale bar is 5 μm. (c) The average aspect ratio of the droplets as a function of cross-sectional area. (d) Actin concentration dependence of average aspect ratio for droplets with areas of 4–6 μm^2 (blue squares), 14–16 μm^2 (red triangles), and >20 μm^2 (black circles). (e–g) Longer actin filaments elongate droplets. All data shown for droplets with 1 μM actin. (e) Fluorescence microscope images of FUS-labeled droplets as a function of droplet size and actin filament length. In the presence of latrunculin (Lat) which prevents actin polymerization, droplets are spherical regardless of size. Scale bar is 5 μm. (f) Aspect ratio as a function of cross-sectional area for droplets containing actin with $L \sim 135$ nm. (g) Average aspect ratio as a function of actin filament length. Symbols are the same as in part (d). Error bars represent ±1 standard deviation between droplets.

We therefore hypothesize that the actin filaments elongate droplet shape through nematic ordering. The resulting nematic elasticity of aligned filaments competes with the droplet interfacial tension, which constrains pure FUS droplets to be spherical. To test whether the filamentous form of actin, rather than the mere actin monomer incorporation, is causing the droplet elongation, we form composite droplets in the presence of the drug latrunculin (Lat) which prevents actin polymerization into filaments. In this case, all droplets are spherical (Fig. 3e). Additionally, previous work has shown that nematic elastic energy scales with the aspect ratio of the rod-like constituents.[12,13] We thus hypothesize that filament length impacts droplet shape. To systematically study the impact of

filament length on droplet shape, we modify the actin filament length through the amount of capping protein.[38] As the concentration of capping protein is increased from 1 mol% to 3 mol%, the average length of the actin filaments is expected to decrease from $\sim$270 nm to $\sim$90 nm. We find that, at 1 μM actin, droplet shape varies with average actin filament length, L, with longer filaments leading to more elongated droplets (Fig. 3e). For $L \sim 135$ nm, smaller (<20 μm^2) droplets are elongated, with the average aspect ratio decreasing with cross-sectional area (Fig. 3f). In contrast, for the shortest actin filaments tested, $L \sim 90$ nm, droplets of all sizes have aspect ratios $\sim$1 (Fig. 3e and g). Notably, for the smallest droplet sizes (4–6 μm^2), the average aspect ratio increases as the filament length increases.
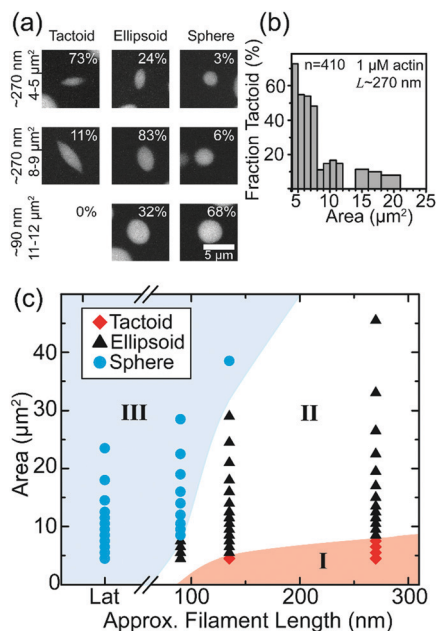
Fig. 4 Droplet size and actin length tune the shape of the droplets. (a) Occurrence of droplet shape for three different droplet cross-sectional areas and filament lengths. Droplets primarily take on one of three shapes: tactoids with pointed tips (left column), ellipsoids that are elongated but have round tips (center), or spheres (right). (b) Fraction of the droplets that are tactoids as a function of cross-sectional area for droplets containing actin with $L \sim 270$ nm. Above 25 μm^2, none of the observed droplets are tactoids. The shape of droplets under 4 μm^2 could not be accurately determined. Bar width corresponds to the range of areas included and varies such that each bar represents at least 10 droplets. (c) Phase space of droplet shape as a function of size and filament length, where latrunculin (Lat) indicates unpolymerized actin. We define three regions based on whether droplets are majority (>50%) tactoids (I, red diamonds), ellipsoids (II, black triangles), or spheres (III, blue circles). All samples contain 1 μM actin and 4.4 μM FUS.

For a given droplet size and composition, there is a distribution of three characteristic shapes: elongated tactoids with pointed ends, ellipsoids, and spheres. The two elongated shapes, tactoids and ellipsoids, are distinguished by the local shape at the tips of the long axis, where tactoids tips are sharp cusps while ellipsoids tips are smooth (Fig. 4a). To quantify the prevalence of these shapes, we measure the fraction of droplets that are tactoids as a function of cross-sectional area. We visually distinguish between tactoids and ellipsoids or spheres based on the droplet tips, noting that even droplets with ellipsoid shape are technically tactoids if they are nematic liquid crystal droplets. With 1 μM actin, $L \sim 270$ nm, droplets with cross-sectional areas less than 8 μm^2 are primarily (>50%) tactoids (Fig. 4b). On the other hand, for larger (>8 μm^2) droplets, the fraction that are tactoids sharply decreases to less than 20%. While the transition from tactoid to ellipsoid and sphere with increasing droplet size has been theoretically predicted,[20,21] to our knowledge it has not been previously experimentally observed. Based on this observation we classify droplets by the shape which is most frequently adopted for each size and filament length. We define any droplet with aspect ratio <1.1 to be a sphere. While in principle this

definition is not mutually exclusive with being a tactoid, we do not observe tactoids with aspect ratios this small. Plotting as a function of filament length and droplet size, we find three regions of phase space (Fig. 4c) based on whether the droplets are primarily (>50%) tactoids (I), ellipsoids (II), or spheres (III). The smallest droplets with longest actin filaments primarily form tactoids (Fig. 4c, Region I). Larger droplets are primarily elliptical, while the largest are spheres (Fig. 4c, Regions II & III). The critical size at which droplet shape transitions to ellipsoids or spheres increases with longer filaments: for $L \sim 90$ nm, all but the smallest (>8 μm^2) sizes are primarily spheres and no droplets are majority tactoids, even at the smallest droplets measured (4 μm^2), while for $L \sim 270$ nm, droplets are primarily ellipsoidal from 8 μm^2 up to the largest size observed (~ 45 μm^2). Droplets containing purely monomeric actin are spherical at all sizes (Fig. 4c, Region III, Lat). Thus, the shape of composite droplets can be tuned either by changing the concentration or length of actin filaments.

At high densities (1 μM) of actin, elongated spindle shaped droplets are seen to nucleate and become more spheroidal as they grow (Fig. 3a and Movie S2, ESI†). This decrease in aspect ratio with increasing droplet size is consistent with the bipolar model of tactoids where the comprising rods (here, actin filaments) align parallel to the droplet interface giving rise to curved director lines that meet at point defects known as "boojums".[20] While these defects are located right at the droplet poles in the ideal bipolar configuration, they can be located off the droplet surface in the more realistic quasi bipolar configuration (Fig. 5a).[34,35] This latter model also successfully describes the continuous transformation of the director geometry from homogeneous, with uniform director lines, to bipolar with increasing droplet size as was previously observed.[14,16] The internal nematic order and its bipolar director orientation for 1 μM actin–FUS droplets is confirmed by observing the droplets under crossed polarizers where intensity corresponds to local nematic order (Fig. 5b). In particular, the reduced intensity seen at the droplet poles suggest the presence of defects in the nematic order that are characteristic of bipolar tactoids.[14] However, the resolution of these polarization images is not sufficient to distinguish between a quasi bipolar and a perfectly bipolar director structure.

The shape and director structure of a nematic tactoid is determined by a balance of its interfacial energy and its bulk nematic elastic energy that depends on the Frank elastic constant, K.[14] The interfacial energy comprises the surface tension, γ, of the droplet, as well as the surface anchoring energy cost of the deviation of the director from parallel alignment with the droplet interface (Fig. 5a). This is expressed by a dimensionless parameter, $\omega = \gamma_A/\gamma$, which is the strength of the surface anchoring energy arising from nematic alignment, γ_A, relative to the fluid surface tension. For a tactoid of characteristic length R, the interfacial energy grows as R^2 with droplet size, whereas the bulk nematic elastic energy scales as R (elastic energy scales as droplet volume times the square of the curvature of the director lines, $R^3 \cdot R^{-2} \sim R$). For bipolar droplets of increasing size, the interfacial energy grows larger relative to
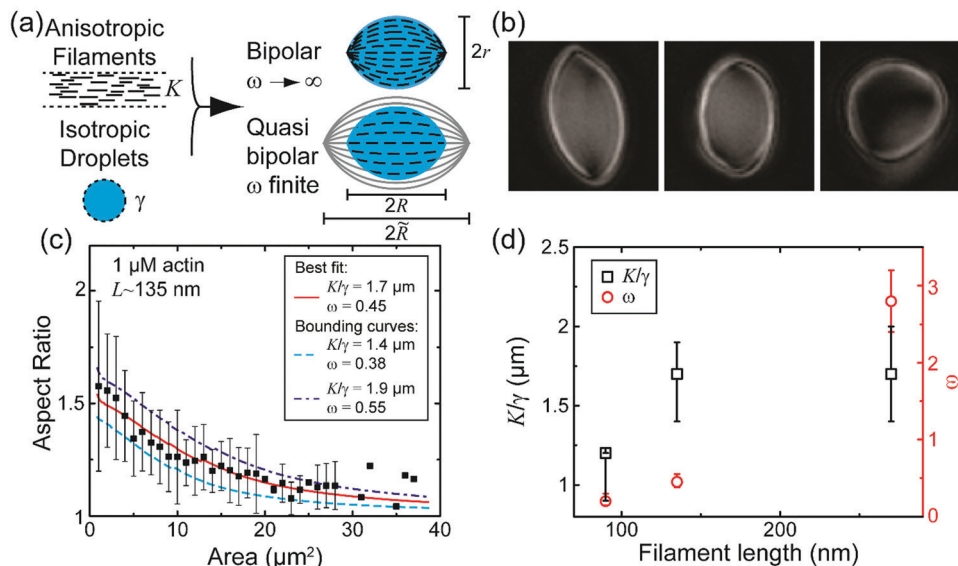
Fig. 5 Bipolar model description of droplet shape. (a) Cartoon schematic of droplet shape determinants. Actin filaments contribute a nematic elastic energy, while FUS droplets predominately contribute an isotropic interfacial energy. Bipolar tactoids have defects at the poles, whereas in quasi bipolar tactoids, virtual defects exist outside the droplet. (b) LC polscope birefringence images of composite droplets. The dark areas at the poles indicate defects lacking local nematic ordering. (c) Theoretical fit (lines) to experimental data (black squares). K/γ and ω are extracted from the best fit (red solid line), while the fits that bound the experimental data give the minimum (light blue dashed line) and maximum (dark blue dashed line) values. Data are from samples containing actin with $L \sim 135$ nm. (d) K/γ (black squared) and ω (red circles) as a function of actin filament length. Error bars are from the maximum and minimum theoretical fits as shown in part (c). All data are from samples containing 1 µM actin.

the bulk elastic energy, resulting in lower aspect ratios that become nearly spherical when the droplet size is large compared to a characteristic nematic distortion length scale, $R \gg K/\gamma$. This behavior is seen for 1 µM actin–FUS tactoids (Fig. 3c). For smaller droplets with $R \ll K/\gamma$, the nematic elastic energy cost of distorting the directors into the bipolar configuration becomes prohibitively expensive resulting in a nearly uniform director structure throughout the droplet. In this homogeneous limit, the aspect ratio of the droplet is determined by the anchoring strength, ω.[20] While continuous transformation of the director structure from homogeneous to bipolar with increasing droplet size was previously reported,[14,16] this transition may occur at droplet sizes below our experimental resolution. The quasi bipolar model captures the droplet shape trends realistically in both these limiting cases and unlike the pure bipolar geometry, it captures the low aspect ratio shapes at small droplet sizes seen in our composite droplets.

Using the quasi bipolar geometry, we numerically minimize the scaled form of the free energy expression to yield expected aspect ratios for a given droplet size, measured as average cross-sectional area in the experiment. In this quasi bipolar model, we expect that the aspect ratio for a given droplet size depends only on two unknown constants: the distortion length scale, K/γ, and the anchoring strength, ω. Comparing the experimental data to the model then lets us estimate average values for both these material properties for the FUS–actin droplets (Fig. 5c and Fig. S1, ESI†). We expect both K/γ and ω to increase with actin concentration as well as average actin filament length, since these parameters drive greater entropic alignment of the actin. This is consistent with previous

experiments in actin nematics that show K scaling with filament length.[12,13] Such trends may also occur in our FUS–actin droplets, but it is not clear given the resolution of our measurements of K/γ (Fig. 5d). The uncertainty in measuring K/γ results from the large dispersion in the observed droplet aspect ratios. Additionally, we estimate the length scale, K/γ, of FUS–actin droplets to be a few microns, similar to estimates from pure actin tactoids,[19] whereas $\omega = \gamma_A/\gamma$ for FUS–actin composite droplets is significantly lower than for pure actin tactoids. This decrease is consistent with the expectation that the presence of FUS increases the interfacial tension but not surface anchoring.

For low densities (0.01 µM) of actin, the resulting droplets are spherical for all sizes, as is expected of pure FUS droplets. This points to the absence of a nematic phase at such low actin concentration. The Onsager theory does in fact predict a critical density of rods above which they align purely on entropic grounds.[9,10] The critical volume fraction at which nematic order occurs scales inversely as the aspect ratio of the filaments, L/D, where $D \sim 8$ nm is the diameter of the constituent actin filaments. This qualitatively explains the observed tendency to form elongated droplets at higher actin concentration as well as at longer average actin filament length. At intermediate densities (0.1 µM), the droplets are slightly elongated and appear ellipsoidal, but their aspect ratio does not depend appreciably on droplet size. They also lack the characteristic pointed ends of a bipolar tactoid. We speculate that this concentration of actin induces some nematic order resulting in a slight anisotropy of the physical properties of the droplet. This results in an ellipsoidal instead of a spherical droplet, while not contributing sufficient nematic order required for the characteristic tactoid shape.

Conclusions

Here we find that actin filaments spontaneously partition into FUS droplets. Since FUS and actin have no known specific biochemical interaction, this suggests the complexation is driven by non-specific protein–protein interactions such as charge or hydrophobicity. Partitioning of filaments induces anisotropy in otherwise isotropic condensates. While it is well appreciated that modifying macromolecular components and their interactions can influence mechanical properties from solid-like to liquid-like in droplets,[7] here we tune the droplet anisotropy while maintaining a liquid phase. Moreover, the partitioning of actin filaments into a significantly reduced volume provides a new route for forming liquid crystal droplets. This complements a growing range of methods to form composite macromolecular droplets, such as previous reported protein partitioning into coacervates due to specific binding interactions[4] or charge interactions.[39–41] Exciting areas of future inquiry may seek to elucidate how the macromolecular component interactions control miscibility and spatial organization of components and mechanics of composite liquid droplets.

One consequence of the droplet's liquid crystallinity is that competing effects of elasticity with interfacial tension give rise to diverse droplet shapes and internal structure. For example, we have shown experimentally the transition between spherical and tactoid-shaped droplets which has been previously theoretically predicted.[20] This shape change inherently causes changes in the surface area to volume ratio, which could be harnessed as a mechanism to dynamically tune partitioning or other interface-mediated activity. Furthermore, these shapes reflect changes in the spatial organization of the filaments across the droplet.[21] This internal structure could be used as a template for droplet-scale spatial structure.[42–45] Thus, composite condensates offer a promising means to understand and design reconfigurable materials where the interfacial and elastic phases can be orthogonally tuned.

Additionally, phase separation is well appreciated as a mechanism of intracellular organization.[46] We speculate that the myriad of biopolymers found within the cytoplasm may spontaneously partition into cytoplasmic condensates to form similar composite droplets *in vivo*. One outstanding example speculated to form a liquid crystalline phase is that of the mitotic spindle.[47] Recently, evidence for a "spindle matrix" comprised of protein-rich condensate around microtubule filaments[48] suggests an analog of the composite we observe. Finally, the extent to which this may influence intermediate filament and actin filament organization is unknown, but has potential implications for neurodegenerative diseases[49] and control of cytoskeletal signaling.[50]

Conflicts of interest

There are no conflicts to declare.

Acknowledgements

References

1 A. B. Marciel, E. J. Chung, B. K. Brettmann and L. Leon, *Adv. Colloid Interface Sci.*, 2017, **239**, 187–198.

2 C. P. Brangwynne, P. Tompa and R. V. Pappu, *Nat. Phys.*, 2015, **11**, 899–904.

3 T. K. Lytle, L. W. Chang, N. Markiewicz, S. L. Perry and C. E. Sing, *ACS Cent. Sci.*, 2019, **5**, 709–718.

4 S. F. Banani, A. M. Rice, W. B. Peeples, Y. Lin, S. Jain, R. Parker and M. K. Rosen, *Cell*, 2016, **166**, 651–663.

5 L. Li, S. Srivastava, M. Andreev, A. B. Marciel, J. J. de Pablo and M. V. Tirrell, *Macromolecules*, 2018, **51**, 2988–2995.

6 X. Wang, J. Lee, Y. W. Wang and Q. Huang, *Biomacromolecules*, 2007, **8**, 992–997.

7 D. V. Krogstad, N. A. Lynd, S. H. Choi, J. M. Spruell, C. J. Hawker, E. J. Kramer and M. V. Tirrell, *Macromolecules*, 2013, **46**, 1512–1518.

8 M. Antonov, M. Mazzawi and P. L. Dubin, *Biomacromolecules*, 2010, **11**, 51–59.

9 L. Onsager, *Ann. N. Y. Acad. Sci.*, 1949, **51**, 627–659.

10 P. G. de Gennes and J. Prost, *The physics of liquid crystals*, Oxford University Press, Oxford, 1995.

11 T. Odijk, *Liq. Cryst.*, 1986, **1**, 553–559.

12 J. P. Straley, *Phys. Rev. A: At., Mol., Opt. Phys.*, 1973, **8**, 2181–2183.

13 R. Zhang, N. Kumar, J. L. Ross, M. L. Gardel and J. J. De Pablo, *Proc. Natl. Acad. Sci. U. S. A.*, 2017, **115**, E124–E133.

14 V. Jamali, N. Behabtu, B. Senyuk, J. A. Lee, I. I. Smalyukh, P. van der Schoot and M. Pasquali, *Phys. Rev. E: Stat., Nonlinear, Soft Matter Phys.*, 2015, **91**, 042507.

15 P. W. Oakes, J. Viamontes and J. X. Tang, *Phys. Rev. E: Stat., Nonlinear, Soft Matter Phys.*, 2007, **75**, 061902.

16 M. Bagnani, G. Nyström, C. De Michele and R. Mezzenga, *ACS Nano*, 2019, **13**, 591–600.

17 A. Modlinska, A. M. Alsayed and T. Gibaud, *Sci. Rep.*, 2015, **5**, 1–10.

18 Y. Trukhina, S. Jungblut, P. Van Der Schoot and T. Schilling, *J. Chem. Phys.*, 2009, **130**, 164513.

19 K. L. Weirich, S. Banerjee, K. Dasbiswas, T. A. Witten, S. Vaikuntanathan and M. L. Gardel, *Proc. Natl. Acad. Sci. U. S. A.*, 2017, **114**, 2131–2136.

20 P. Prinsen and P. van der Schoot, *Phys. Rev. E: Stat., Nonlinear, Soft Matter Phys.*, 2003, **68**, 11.

21 R. M. W. Van Bijnen, R. H. J. Otten and P. Van Der Schoot, *Phys. Rev. E: Stat., Nonlinear, Soft Matter Phys.*, 2012, **86**, 1–12.

22 G. Nyström, M. Arcari and R. Mezzenga, *Nat. Nanotechnol.*, 2018, **13**, 330–336.

23 P. X. Wang and M. J. MacLachlan, *Philos. Trans. R. Soc., A*, 2018, 376.

24 J. Brugués and D. Needleman, *Proc. Natl. Acad. Sci. U. S. A.*, 2014, **111**, 18496–18500.

25 W. Heller, W. Wojtowicz and J. H. L. Watson, *J. Chem. Phys.*, 1948, **16**, 998–999.

26 A. Patel, H. O. Lee, L. Jawerth, S. Maharana, M. Jahnel, M. Y. Hein, S. Stoynov, J. Mahamid, S. Saha, T. M. Franzmann, A. Pozniakovski, I. Poser, N. Maghelli, L. A. Royer, M. Weigert, E. W. Myers, S. Grill, D. Drechsel, A. A. Hyman and S. Alberti, *Cell*, 2015, **162**, 1066–1077.

27 J. A. Spudich and S. Watt, *J. Biol. Chem.*, 1971, **246**, 4866–4871.

28 S. Palmgren, P. J. Ojala, M. A. Wear, J. A. Cooper and P. Lappalainen, *J. Cell Biol.*, 2001, **155**, 251–260.

29 J. Xu, J. F. Casella and T. D. Pollard, *Cell Motil. Cytoskeleton*, 1999, **42**, 73–81.

30 R. Oldenbourg, *Nature*, 1996, **381**, 811–812.

31 C. A. Schneider, W. S. Rasband and K. W. Eliceiri, *Nat. Methods*, 2012, **9**, 671–675.

32 J. Schindelin, I. Arganda-Carreras, E. Frise, V. Kaynig, M. Longair, T. Pietzsch, S. Preibisch, C. Rueden, S. Saalfeld, B. Schmid, J.-Y. Tinevez, D. J. White, V. Hartenstein, K. Eliceiri, P. Tomancak and A. Cardona, *Nat. Methods*, 2012, **9**, 676–682.

33 A. V. Kaznacheev, M. M. Bogdanov and S. A. Taraskin, *J. Exp. Theor. Phys.*, 2002, **95**, 57–63.

34 P. Prinsen and P. Van Der Schoot, *Eur. Phys. J. E*, 2004, **13**, 35–41.

35 R. D. Williams, Rutherford Applet. Lab. Rep., 1985, RAL-85-028.

36 S. F. Banani, A. M. Rice, W. B. Peeples, Y. Lin, S. Jain, R. Parker and M. K. Rosen, *Cell*, 2016, **166**, 651–663.

37 P. M. McCall, S. Srivastava, S. L. Perry, D. R. Kovar, M. L. Gardel and M. V. Tirrell, *Biophys. J.*, 2018, **114**, 1636–1645.

38 A. Weeds and S. Maciver, *Curr. Opin. Cell Biol.*, 1993, **5**, 63–69.

39 K. A. Black, D. Priftis, S. L. Perry, J. Yip, W. Y. Byun and M. Tirrell, *ACS Macro Lett.*, 2014, **3**, 1088–1091.

40 A. C. Obermeyer, C. E. Mills, X. H. Dong, R. J. Flores and B. D. Olsen, *Soft Matter*, 2016, **12**, 3570–3581.

41 C. W. Pak, M. Kosno, A. S. Holehouse, S. B. Padrick, A. Mittal, R. Ali, A. A. Yunus, D. R. Liu, R. V. Pappu and M. K. Rosen, *Mol. Cell*, 2016, **63**, 72–85.

42 K. L. Weirich, K. Dasbiswas, T. A. Witten, S. Vaikuntanathan and M. L. Gardel, *Proc. Natl. Acad. Sci. U. S. A.*, 2019, **116**, 201814854.

43 P. Poulin, H. Stark, T. C. Lubensky and D. A. Weitz, *Science*, 1997, **275**, 1770–1773.

44 X. Wang, D. S. Miller, J. J. De Pablo and N. L. Abbott, *Soft Matter*, 2014, **10**, 8821–8828.

45 P. X. Wang, W. Y. Hamad and M. J. MacLachlan, *Angew. Chem., Int. Ed.*, 2018, **57**, 3360–3365.

46 A. A. Hyman, C. A. Weber and F. Jülicher, *Annu. Rev. Cell Dev. Biol.*, 2014, **30**, 39–58.

47 J. Brugués and D. Needleman, *Proc. Natl. Acad. Sci. U. S. A.*, 2014, **111**, 18496–18500.

48 H. Jiang, S. Wang, Y. Huang, X. He, H. Cui, X. Zhu and Y. Zheng, *Cell*, 2015, **163**, 108–122.

49 N. J. Cairns, V. M.-Y. Lee and J. Q. Trojanowski, *J. Pathol.*, 2004, **204**, 438–449.

50 X. Su, J. A. Ditlev, E. Hui, W. Xing, S. Banjade, J. Okrut, D. S. King, J. Taunton, M. K. Rosen and R. D. Vale, *Science*, 2016, **352**, 595–599.